Interaction of an inner-scaled Helmholtz resonator with boundary-layer turbulence

Hassanein, Abdelrahman; Modesti, Davide; Scarano, Fulvio; Baars, Woutijn J.

Important note
To cite this publication, please use the final published version (if applicable).
Please check the document version above.

Interaction of an inner-scaled Helmholtz resonator with boundary-layer turbulence

Abdelrahman Hassanein ⓘ,[*] Davide Modesti ⓘ, Fulvio Scarano ⓘ, and Woutijn J. Baars ⓘ
Faculty of Aerospace Engineering, Delft University of Technology, 2629 HS Delft, The Netherlands

We investigate the impact of a single miniature Helmholtz resonator on wall-bounded turbulence using time-resolved planar particle image velocimetry. A particular aim is to explain the mechanism by which a resonator alters the turbulent velocity fluctuations of different scales. A grazing flow configuration is studied in which the resonator is embedded in the wall beneath a turbulent boundary layer at a friction Reynolds number of $\mathrm{Re}_\tau \approx 2300$; the resonator is designed so that its resonance frequency matches the peak frequency of the wall-pressure spectrum. It is found that the resonator amplifies velocity fluctuations near its resonance frequency, while it attenuates the energy of subresonance scales. Underlying mechanisms responsible for these changes in energy are discussed in view of the resonator's local impedance condition. It is posited that large-scale velocity fluctuations in the wall-normal velocity, at temporal frequencies below resonance, are subject to a phase-opposed wall-normal velocity perturbation when the TBL flow convects over the resonator's orifice. This yields a decrease of large-scale energy in $\overline{u'u'}$, $-\overline{u'v'}$, and $\overline{v'v'}$. In addition, modifications of the wall-shear stress field downstream of the resonator are addressed. Insights from this research will contribute to the development of surface designs for passive skin-friction control using arrays of miniature resonators.

I. INTRODUCTION

Wall-bounded turbulence and its interactions with different surfaces have been an active area of research for over four decades. Motives behind these studies vary, but chief among them is the substantially positive economic and environmental impact that said research has when control of turbulence leads to skin-friction drag reduction. In the current work, we focus on a wall-embedded Helmholtz resonator (HR), since resonators have shown promise in manipulating near-wall turbulence by altering the scale-dependent wall impedance condition [1–4]. By concentrating on a miniature HR, scaled to interact with the near-wall region of a turbulent boundary layer (TBL), we will study the fundamental physics of the resonator-turbulence interaction. Findings will inspire the possible application of HRs as array elements in the design of surfaces for affecting wall-bounded turbulence.

Even though fully developed wall-bounded turbulence is broadband in nature, it contains a degree of structure that will govern the resonance-turbulence interaction. A self-sustained near-wall cycle in the buffer region is most intense at a wall-normal distance of $y^+ \approx 15$, where the peak of the production of near-wall turbulence appears [5,6]. Here, the superscript "+" denotes a viscous scaling using length scale $l_v = \nu/U_\tau$, formed from the friction velocity, $U_\tau = \sqrt{\tau_w/\rho}$, and the kinematic viscosity of the fluid, ν (note that τ_w is the wall-shear stress and ρ is the fluid density). Even though the $y^+ \approx 15$ peak location is constant with changes of the friction Reynolds number $\mathrm{Re}_\tau \equiv \delta/l_v$ (where δ is the boundary-layer thickness), the bulk of the production

---

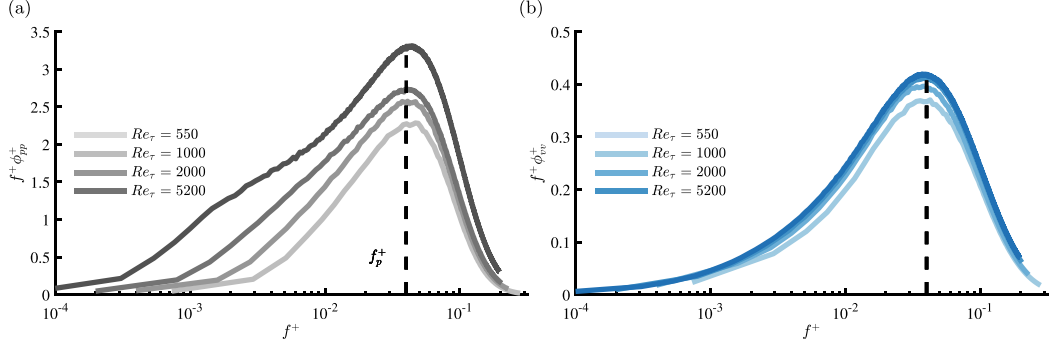[*]Contact author: a.h.hassanein@tudelft.nl

FIG. 1. Energy spectra at different values of Re_τ for the (a) wall-pressure fluctuations and (b) wall-normal velocity fluctuations at $y^+ = 100$. Spectra are taken from direct numerical simulations of turbulent channel flow [7]; note that the wavelength axes from the spatial simulation data are here converted into frequency axes using $f^+ = U_c^+/\lambda_x^+$ (with $U_c^+ = 10$).

of turbulence kinetic energy shifts towards the logarithmic region with an increasing value of Re_τ [6]. Regardless of a stronger wall-imprint of larger-scale turbulence at higher Re_τ conditions, the streamwise velocity fluctuations remain most energetic at a streamwise wavelength of $\lambda_x^+ = 1000$, and those of the wall-normal velocity and wall-pressure fluctuations contain the most energy around $\lambda_x^+ = 250$. Figure 1 highlights these features by showing energy spectra at four different Re_τ of the (a) wall-pressure fluctuations and (b) wall-normal velocity fluctuations at $y^+ = 100$, obtained from direct numerical simulations of turbulent channel flow [7,8]. The aforementioned inner-scaled wavelengths associated with the spectral peaks are spatial ones, but experimental works revealed the same Reynolds number invariance of the inner-spectral peak of temporal spectra, residing at a frequency of $f_p^+ \approx 0.04$ [e.g., 9,10] (here the subscript "p" signifies the peak). This implies that f_p^+ and $\lambda_{x,p}^+$ are related at the peak scale through a convection velocity of $U_c^+ \approx 10$. Because our study concentrates on resonators that are tuned towards the peak of the wall-pressure spectrum, it is envisioned that our findings are valid for other values of Re_τ, provided that the resonator-turbulence interaction is governed by viscous scaling.

In our current study, we assess the impact of a HR interacting with near-wall turbulence. Panton and Miller [11] were the first to investigate the acoustic response of grazing TBL flow over small HRs tuned to different parts of the wall-pressure spectrum. Subsequent studies by Panton *et al.* [1], Flynn *et al.* [2], and Flynn and Panton [3] partially addressed the impact of these resonators on turbulence, wherein they show an increase in the streamwise and wall-normal velocity fluctuations but minimal changes in cross-stream velocity fluctuations. However, the exploration did not endeavor into the extent to which resonators affect the energy distribution across different turbulence scales. Dacome *et al.* [4] did focus on this by independently varying the inner-scaled orifice diameter and resonance frequency. They found that the streamwise velocity fluctuation energy was amplified downstream of the resonator, near the resonance frequency. This amplification coexisted with a reduction in larger-scale energy of the streamwise velocity fluctuations. These energy changes were more pronounced when the resonator's natural frequency aligned closely with the peak frequency of the wall-pressure spectrum. Unique to our current study is that time- and space-resolved data is available. This allows not only for an assessment of the energy spectra, but also for an inspection of the mechanisms by which the convecting turbulent velocity fluctuations interact with the resonator physics on a per-frequency basis.

A. Fundamentals of Helmholtz resonators

Generally, a HR comprises an orifice and a cavity, which in the case of a cylindrical resonator are parameterized by the orifice diameter d and thickness l, and cavity diameter D and length
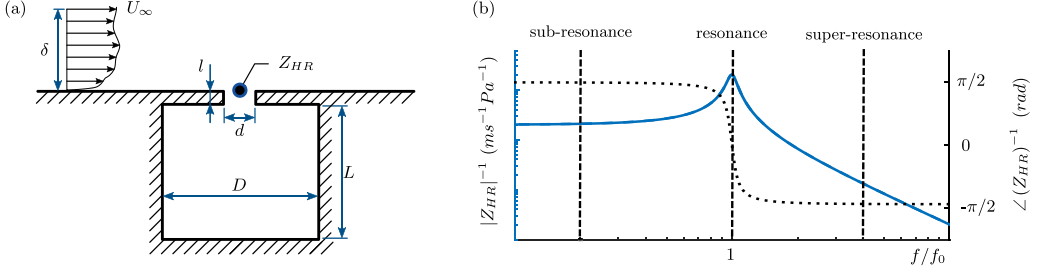
FIG. 2. (a) Schematic of a cylindrical Helmholtz resonator (HR) beneath a grazing TBL flow. (b) Gain curve (solid) and phase curve (dotted) of the acoustic impedance-inverse of a single HR.

L [see Fig. 2(a)]. The orifice and cavity cross-sectional areas are denoted as $s = \pi d^2/4$ and $S = \pi D^2/4$, respectively, and $V = SL$ is the cavity volume. Using a mass-spring analogy, the resonator's natural frequency can be derived by modeling the system with a second-order differential equation governing air displacement in the y direction [12]:

$$f_0 = \frac{a_0}{2\pi} \sqrt{\frac{s}{V(l + l^*) + P}}. \tag{1}$$

Here, a_0 is the speed of sound, and terms l^* and P are "end corrections" accounting for air-mass displaced by the neck's air-mass on either side of the orifice [13]. Here we adopt end corrections $l^* = l^*_{in} + l^*_{out} = 0.48\sqrt{s}(1 - 1.25d/D) + 0.48\sqrt{s}$ [13] and $P = L^2 s/3$ [14], as they were shown to provide a reasonable approximation of f_0 in both the absence and presence of grazing flow [4]. At the orifice of the HR, wall-normal velocity fluctuations will be induced as a response to imposed pressure fluctuations. The ratio between the pressure at the orifice, p_o, exciting the resonator, and the resultant wall-normal velocity fluctuations, v_o, is frequency dependent. This relation is known as the acoustic impedance, $Z_{HR} \equiv P_o(f)/V_o(f)$. Note that capital quantities P and V signify the temporal FFT of signals p and v, respectively. Typical gain and phase curves of the acoustic impedance are drawn in Fig. 2(b), illustrating that the spectral response of an HR can be classified into three regimes: subresonance, resonance, and super-resonance. Under pressure excitation, the resonator will amplify a narrow band of pressure waves within the cavity with frequencies close to resonance. Consequently, the oscillating mass flux through the resonator's orifice will amplify around resonance. As for the temporal phase relation, the wall-normal velocity precedes the orifice pressure by a quarter-period for frequencies below resonance. At resonance, the wall-normal velocity and the pressure at the center of the orifice fluctuate in phase. Beyond resonance, the pressure at the orifice leads the wall-normal velocity by a quarter-period. In addition to the acoustic impedance of a HR, the resonator's transfer kernel of pressure is generally used to infer the strength of resonance. This frequency-dependent kernel relates the cavity pressure to the pressure within the orifice, following $H_{HR} \equiv P_c(f)/P_o(f)$.

B. Present contribution and outline

Given the scale-dependent nature of the resonator interacting with boundary-layer turbulence, spatiotemporal information of the grazing velocity fluctuations is required to fully describe the physics of the resonator-turbulence interaction. In particular, this paper aims to reveal the physical mechanism causing attenuation of large-scale energy downstream of the resonator [4]. For accomplishing this, our study revolves around an experiment using time-resolved particle image velocimetry (TR-PIV), providing spatiotemporal data. These data allow for assessing changes in turbulence statistics—like the spectral energy—above and downstream of the HR. In addition, it permits the construction of a scale-dependent view of the resonator-turbulence interaction. Finally,
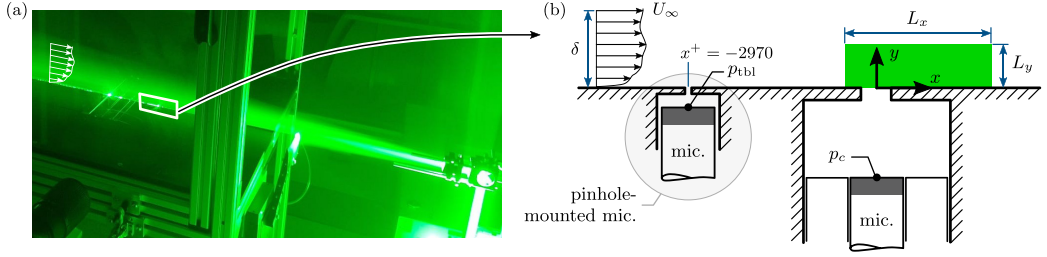
FIG. 3. (a) Photograph of the TR-PIV setup. (b) Schematic of the pinhole-mounted microphone and the HR, along with the field of view of the TR-PIV measurement. Also indicated are the locations of the two microphones for measuring the fluctuating pressures, p_{tbl} and p_c.

the impact of the resonator-turbulence interaction on the wall-shear stress is assessed with oil film interferometry (OFI), so that the possibility of utilizing local changes in wall impedance is explored as a drag-reducing technology in wall-bounded turbulence.

Section II begins with a description of the experimental flow facility, followed by an outline of the methodology, key features of our baseline TBL flow, and properties of the HR. Section III provides a breakdown of how the resonator affects the TBL statistics. First, observations and changes within the instantaneous and mean flow fields are presented. This is followed by an assessment of the spectral energy content of the velocity fluctuations, as well as the distribution of wall-shear stress downstream of the resonator. Section IV elaborates on the underlying physics of the resonator-turbulence interaction, by concentrating on the convective fluctuations and HR-induced perturbations.

II. EXPERIMENTAL METHODOLOGY

A. Flow facility

A TBL was generated in a low-speed open-return wind tunnel facility (W-tunnel) at the Delft University of Technology, comprising a cross section of $0.60 \times 0.60\,\text{m}^2$ at the inlet of the test section. The TBL developed over a flat plate with a spanwise width of 0.60 m and a total streamwise length of 3.75 m under zero-pressure gradient conditions. The transition was forced (on all sides) using P40-grain sandpaper at the start of the leading edge. Further details of the facility are described by Baars *et al.* [15]. An (x, y) coordinate system is defined at the center of the HR's orifice, located at 3.17 m from the leading edge and in the spanwise center of the test section. This coordinate system is adopted when presenting results in upcoming sections. In the remainder of this paper, data is presented corresponding to two cases: (i) without the resonator being present (referred to as the "baseline" case), and (ii) with the resonator being installed (referred to as the "HR" case).

B. Flow measurements and instrumentation

Fluctuating pressure measurements were conducted with the aid of GRAS 46BE 1/4-in pressure microphones at two positions as indicated in Fig. 3(b): (i) within the wall, 90 mm upstream of the resonator, for measuring the wall-pressure signature of the incoming boundary layer p_{tbl}, and (ii) at the bottom of the resonator's cavity to capture the cavity pressure p_c. The wall-embedded microphone utilized a pinhole configuration (in essence forming a HR so that the relatively small orifice size causes an enhancement of the spatial resolution of the sensor). Dimensions of the pinhole were $d = 0.4\,\text{mm}$, $l = 1.0\,\text{mm}$, $D = 6.0\,\text{mm}$, and $L = 2.0\,\text{mm}$, which yielded a natural frequency of 2725 Hz. The pressure signal p_{tbl} was then corrected using the Helmholtz correction (see Appendix A in [15]). The microphone sets possess a nominal sensitivity of 3.6 mV/Pa and maintain an accurate frequency response within ± 1 decibel (dB, with a reference pressure of 20 μPa) in the range from 10 Hz to 40 kHz. The dynamic range spans from 35 to 160 dB.

High-speed PIV was used to obtain spatiotemporal velocity fields in the near vicinity of the resonator's orifice. Water-glycol droplets of 1 μm diameter were produced with a SAFEX smoke generator; seeding was inserted in the wind tunnel and circulated in the laboratory until the desired concentration was achieved. Illumination was provided with a Quantronix Darwin-Duo 527 Nd:YLF laser (2×25 mJ @ 1 kHz). The thickness of the laser sheet was kept to 1 mm. Imaging was conducted using a Photron FASTCAM SA1.1 (1024×1024 px^2 at 5.4 kHz, and a 20-μm pixel size). During the measurement, the active sensor area was cropped to 750×512 px^2 to allow a higher acquisition frequency. This yielded a field-of-view of 14×9.5 mm^2, or in viscous scaling one obeying a length of $L_x^+ \approx 460$ and a height of $L_y^+ \approx 310$ [see Fig. 3(b)]. A Nikon lens with a 200-mm focal length and an aperture $f_\#$ of 4 was used, along with a teleconverter to double optical magnification. The resulting image resolution was 53.7 px/mm (1 px $= 1.86$ μm $= 0.6 l_v$). With the active sensor area, the acquisition frequency was set to 14.94 kHz, resulting in a time separation of 67 μs between subsequent frames. For both the baseline and HR cases, PIV datasets comprised a total of 86 400 images, divided into six ensembles of 14 400 uninterrupted image sequences.

LaVision's DAVIS 10.2 software was utilized for system synchronization, image acquisition, and PIV processing. The cross-correlation of the time-resolved recordings is performed with the sliding sum-of-correlations technique [16], with a length of four frames to reduce measurement noise and increase the robustness of correlation peak detection. The cross-correlation makes use of the multi-grid window deformation method, with a window size for the final interrogation step of 24×6 px^2 with 75% overlap. The interrogation area is stretched in the streamwise direction and reduced in the wall-normal direction to increase spatial resolution in the latter direction. Adjacent vectors are returned with a pitch of 3 px (corresponding to a vector pitch in wall-normal direction of $\Delta y^+ \approx 2$). See Table I for a summary of the PIV measurement and postprocessing parameters. Finally, for each PIV dataset, fluctuating pressure measurements were conducted in a synchronized manner with a sampling frequency of 51.2 kHz. With the synchronized recording of the laser's Q-switch signal and the microphone pressure recordings, the dataset allows for conditioning PIV-based velocity fields based on events of fluctuating pressure.

Convergence of turbulence statistics, such as the variance, stands out as a significant error source in TR-PIV. To assess its impact on results, the variation in streamwise Reynolds stress was analyzed across varying sample sizes. This analysis targeted the most intense fluctuations in the wall-normal region around $y^+ = 15$ and revealed that a minimum of 50×10^3 images is imperative for the streamwise Reynolds stress to converge within 1% of its ultimate value. This convergence is benchmarked against a total of (86×10^3) images, establishing the reliability of the results.

OFI measurements were conducted to quantify the wall-shear stress modifications. The apparatus included a Nikon D5600 camera and lens, featuring a 180 mm focal length and an aperture $f_\#$ of 8. The camera was inclined so that the viewing angle was at 43.3 degrees relative to the wall within the (y, z) plane; a calibration procedure was performed to obtain the image resolution of 21.4 px/mm. For illumination, a monochromatic sodium lamp emitting light with a wavelength of $\lambda_{\text{sod}} = 589$ nm was employed [see Fig. 4(a)]. A XIAMETER$^{\text{TM}}$ PMX-200 silicone fluid with a viscosity of 100 cSt was used to create three droplets: two of these were placed on either spanwise side of the resonator (used as baseline reference), about 10 mm away from the HR's orifice, and one was placed exactly downstream of the HR. Time-lapse data of the oil film spreading comprised a total of 100 images, acquired with a five-second interval. The acquisition process commenced once the droplets formed a sufficiently thin film so that the fringes were visible. Additionally, the surface temperature was acquired with thermocouples at a rate of 3 Hz.

In postprocessing OFI data, an interrogation window of 4×70 px^2 was selected to ensure it encompassed a minimum of four fringes [Fig. 4(b) displays an image of the OFI with one postprocessing window indicated]. The wall-shear stress can be inferred through the following

TABLE I. PIV measurement and postprocessing parameters.

Laser sheet	
Laser type	Nd:YLF
Manufacturer	Quantronix
Model	Darwin-Duo 527
Maximum energy	2×25 mJ @ 1 kHz
Wavelength	527 nm
Thickness	1 mm
Time between pulses	67 μs
Camera	
Model	Photron FASTCAM SA1.1
Sensor resolution	756×512 px^2
Pixel pitch (size)	20 μm
A/D conversion	12 bit
Acquisition rate	14 940 fps
Seeding	
Type	Atomized water-glycol
Nominal diameter	1 μm
Imaging conditions and analysis	
Field of view	14×9.5 mm^2
Image resolution	53.7 px/mm
Interrogation window	24×6 px^2
Processing technique	Sliding sum of correlation
Overlap	75%
Vector pitch	0.056 mm, $\Delta y^+ \approx 2$

formulation [17]:

$$\tau_w = \frac{2\mu_{\text{oil}}\sqrt{n_{\text{oil}}^2 - n_{\text{air}}^2 \sin^2 \theta}}{\lambda_{\text{sod}}} \frac{\Delta x}{\Delta t}, \tag{2}$$

where μ_{oil} is the viscosity of the oil, n_{oil} is the refractive index of the oil, n_{air} is the refractive index of air, θ is the viewing angle of the camera, and λ_{sod} is the wavelength of the light source. Additionally, $\Delta x/\Delta t$ is the fringe velocity, which was found from the time rate of change of the fringe spacing.
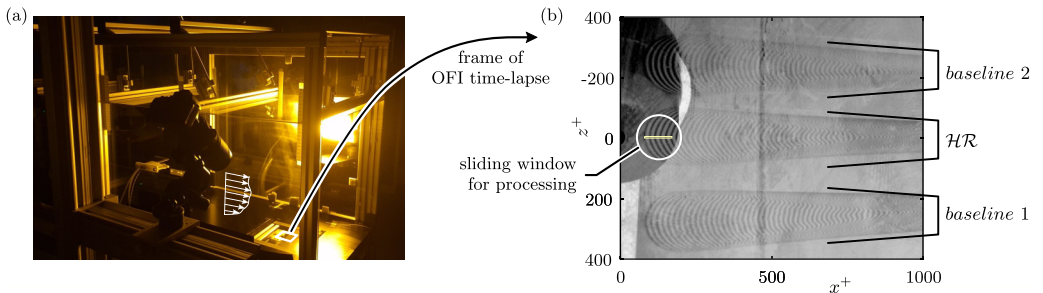

FIG. 4. (a) Photograph of the OFI setup. (b) A sample frame of the OFI time lapse, showing three oil films: one downstream of the resonator ($\mathcal{HR}$), and two to the sides for measuring the baseline flow (*baseline* 1 and 2). A sample of the sliding interrogation window used for postprocessing is also indicated.

TABLE II. Nominal parameters of the baseline TBL flow.

U_∞(m/s)	Re_τ	δ(mm)	U_τ(m/s)	$l_v \equiv \nu/U_\tau$(μm)	$t_v \equiv \nu/U_\tau^2$(μs)
15	2300	72.0	0.52 ± 0.01	30.3 ± 0.5	57 ± 2

The wall-shear stress was mapped behind the resonator at five spanwise positions: $z^+ = [-30 : 15 : 30]$. For each of the selected positions, a sliding window in the streamwise direction with 50% overlap was employed to cover the range $x^+ = [95 : 45 : 320]$. Not only was the wall-shear stress inferred from the spanwise center position of the oil film but also from various off-center positions in the span. This is feasible because the transverse curvature of the fringes does not change in the streamwise direction [18]. In presenting the wall-shear stress data, the center of each interrogation window is chosen to represent the position of the window. In addition, the interrogation windows were chosen to be sufficiently far from the oil film's edges. As for the baseline case, a single value of the wall-shear stress is reported from averaging the results corresponding to the two oil films on either side (labeled *baseline*1 and 2). Each film was postprocessed with three spanwise positions per film, and with a sliding window similar to that used for processing the film behind the resonator.

In order to quantify the measurement uncertainty of the OFI measurements, we employed an *a posteriori* uncertainty quantification. In general, the uncertainty in the OFI technique can arise from different factors [19], with the most prominent ones originating from the peak identification, the linear fit used to obtain the growth rate of the fringes, and the uncertainty in the oil's viscosity. Here, we make use of the skin-friction coefficient obtained from the droplets that represent the baseline TBL, where the standard error calculated using the total 36 sample points equals 3%.

C. Turbulent boundary-layer characteristics

All flow field data are presented using the friction velocity inferred from the OFI measurement of the baseline flow [*baseline* 1 and 2 in Fig. 4(b)]. Throughout the remainder of the paper, this friction velocity (and corresponding viscous length and timescales) will be used when presenting results with an inner normalization, including those of the case with the HR installed. Table II summarizes the TBL parameters. Note that the boundary-layer thickness, δ, and the friction Reynolds number, Re_τ, were inferred from wall-normal profiles of hot-wire measurements, of which the details are reported by Dacome *et al.* [4].

Key characteristics of the baseline TBL are now presented based on the TR-PIV data. Profiles of the mean velocity and several Reynolds stresses are presented in Figs. 5(a) and 5(b). PIV data are in agreement with the data points of the hot-wire measurements, as well as with DNS data of turbulent channel flow, taken from Lee and Moser [7], at an almost identical Reynolds number. For the wall-normal distribution of the Reynolds shear stress $\overline{u'v'}$ and the normal Reynolds stress $\overline{v'v'}$, close agreement with the reference data is shown. An apparent attenuation in energy is observed in the streamwise Reynolds stress $\overline{u'u'}$, obtained with both PIV and hot-wire anemometry, in comparison to the DNS data. This is the consequence of spatial filtering by the relatively large interrogation window size (in the streamwise direction) used in PIV postprocessing and the spatial filtering due to the sensing length in the case of the hot-wire anemometry measurements [20]. This attenuation does not affect findings of our current study, because findings of the case with the HR installed are compared to identical measurements made on a baseline flow.

From the TR-PIV data, spectrograms of the streamwise velocity, wall-normal velocity fluctuations, and the cospectrogram of the streamwise and wall-normal velocity fluctuations are shown in Figs. 6(a)–6(c), respectively. Here, one-sided streamwise spectra were taken as $\phi_{uu}(y; f) = 2\langle \widehat{U}(y; f)\widehat{U}^*(y; f)\rangle$, with $\widehat{U}(y; f)$ indicating the temporal Fourier transform, angular brackets $\langle . \rangle$ indicating ensemble averaging, and superscript * indicating the complex conjugate. Ensemble averaging was employed with ensembles of $N = 2^{10}$ and a Hanning window with a 50% overlap.
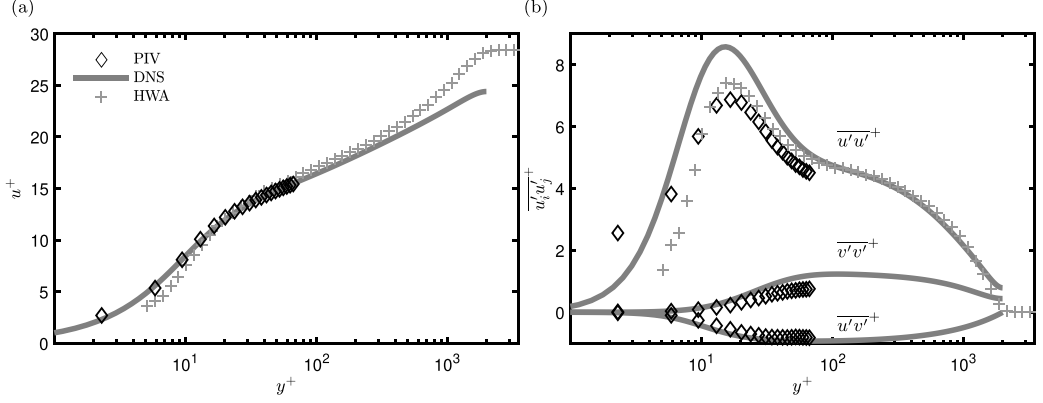
FIG. 5. (a) Streamwise mean velocity profile and (b) profiles of relevant Reynolds stress components of the PIV measurements, compared to hot-wire anemometry (HWA) measurements in the same facility and for the same flow conditions. Experimental data is compared to DNS data of a turbulent channel flow at $\mathrm{Re}_\tau \approx 2000$ [7]. To avoid overclustering of the symbols, only every other PIV data point is plotted.

Finally, a bandwidth moving filter of 20% band was applied before constructing the spectrogram in (f^+, y^+) space.

For the u spectrogram in Fig. 6(a), the inner spectral peak is well captured with the TR-PIV at the expected location of $(y^+; f^+) = (15; 0.01)$. Much less energetic v fluctuations are also well captured, showcased by the v spectrogram exhibiting an inner spectral peak at $(y^+; f^+) \approx (100; 0.04)$ [recall Fig. 1(b)]. In addition, the cospectrogram of the streamwise and wall-normal velocity fluctuations yields the expected inner-spectral peak at $(y^+; f^+) \approx (50; 0.02)$ [7].

D. Helmholtz resonator characteristics

Dimensions of the resonator followed from the work of Dacome *et al.* [4] and are listed in Table III. An orifice diameter of $d^+ = 60$ was selected to ensure that the viscous losses in the orifice are not excessively large and weaken the ability of the resonator to affect the flow. Other dimensions of the resonator were chosen such that its natural frequency matches the peak frequency
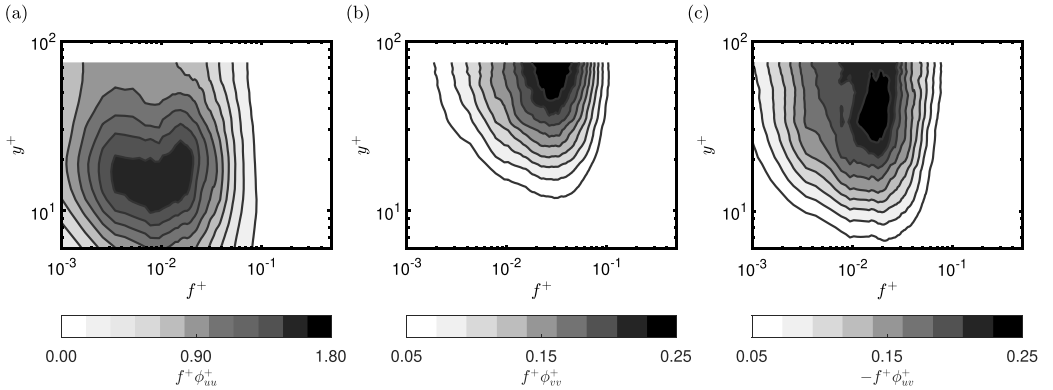

FIG. 6. Premultiplied energy spectrogram of (a) streamwise velocity fluctuations $f^+\phi_{uu}^+$ and (b) wall-normal velocity fluctuations $f^+\phi_{vv}^+$. (c) Premultiplied energy cospectrogram of streamwise and wall-normal velocity fluctuations $-f^+\phi_{uv}^+$.

TABLE III. Properties of the Helmholtz resonator.

d (mm)	l (mm)	D (mm)	L (mm)	f_0 (Hz)	f_0/f_p
1.8	2.4	13	22.7	723	1

of the wall-pressure spectrum ($f_p^+ \approx 1/25$). This choice of resonance frequency guarantees that broadband spectra of wall-pressure and velocity fluctuations in the grazing TBL flow are affected by the different regimes of the HR's impedance condition, as outlined in Sec. I A.

To validate the characteristics of the employed resonator, the gain of the resonator's transfer kernel, Eq. (3), as well as the gain of the impedance, Eq. (4), were inspected:

$$|H_{\mathrm{HR}}| = \sqrt{\frac{\langle P_c(f)P_c^*(f)\rangle}{\langle P_{\mathrm{tbl}}(f)P_{\mathrm{tbl}}^*(f)\rangle}}, \quad \text{and} \tag{3}$$

$$|Z_{\mathrm{HR}}| = \sqrt{\frac{\langle P_{\mathrm{tbl}}(f)P_{\mathrm{tbl}}^*(f)\rangle}{\langle V_o(f)V_o^*(f)\rangle}}. \tag{4}$$

The gain of the transfer kernel is inferred from the incident pressure and cavity pressure. Since the incident pressure cannot be measured at the orifice, the signal p_{tbl} is used as a surrogate; this is sufficient for the gain (but not for inferring the phase relation, because p_{tbl} and p_c are not colocated). The impedance gain is computed using the same incident pressure signal, p_{tbl}, and the *effective* wall-normal velocity fluctuations across the orifice, v_o. These latter fluctuations are generated by box-averaging the wall-normal velocity in a region just above the resonator ($x = [-0.5d, 0.5d]$ and $y = [0, 0.1d]$).

For ensemble averaging the frequency-dependent relations, ensembles of length $N = 2^{11}$ were taken from the time series with 50% overlap. Figures 7(a) and 7(b) show the gain of both the inverse of the impedance and the HR's transfer kernel. Resonance is evident from the appearance of a strong peak near $f = 723$ Hz. Moreover, one can observe an overtone in Fig. 7(b), of which the peak frequency can be obtained analytically by solving the wave-tube equations [14]. However, the small amplitude and very high frequency render its effect negligible on the flow.

III. RESULTS

A. Instantaneous flow features

We start by inspecting the instantaneous velocity fluctuations in close proximity to the HR at specific time instances corresponding to an inflow and outflow phase. Figures 8(a) and 8(b) show contours of the instantaneous streamwise velocity fluctuation u' and the instantaneous wall-normal velocity v during an inflow phase of the resonator cycle. Conversely, the velocity contours are
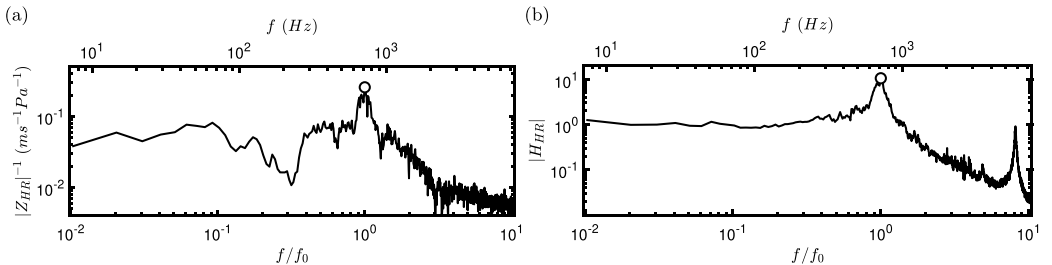

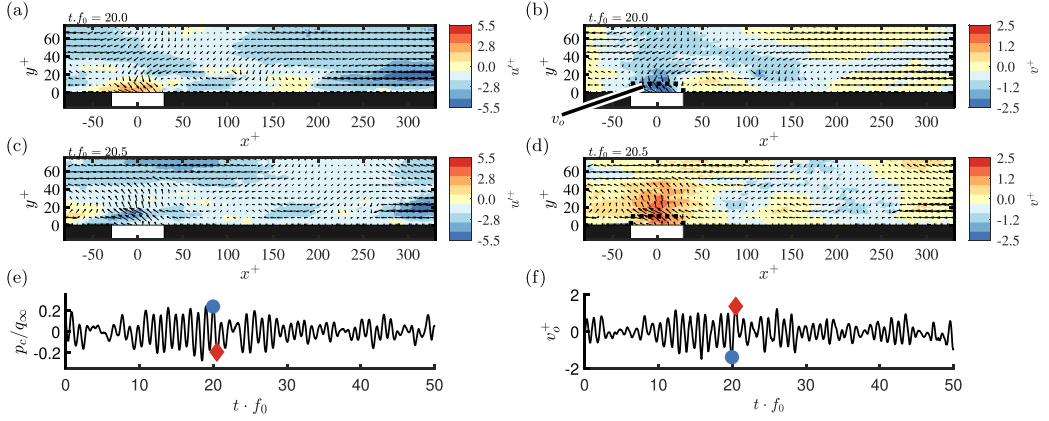FIG. 7. The gain response of (a) the impedance inverse and (b) the HR's transfer kernel.

FIG. 8. (a), (b) Contours of the instantaneous streamwise velocity fluctuation u'^{+} and the instantaneous wall-normal velocity v^{+} during (a), (b) an inflow phase and (c), (d) an outflow phase, respectively. (e) Time series of the cavity pressure with the instances corresponding to the resonator inflow (blue circle) and resonator outflow (red diamond) marked. (f) Identical to subfigure (e) but for the wall-normal velocity across the orifice.

shown in an identical manner for an outflow phase in Figs. 8(c) and 8(d). For reference, the time series of the cavity pressure and the effective wall-normal velocity above the HR, are shown in Figs. 8(e) and 8(f), respectively. A video of the instantaneous streamwise velocity fluctuation u'^{+}, the instantaneous wall-normal velocity v^{+}, and simultaneous time series of the cavity pressure and wall-normal velocity across the orifice is provided in the Supplemental Material [21]. Qualitative observations of the velocity fluctuations are in line with the phase-average analysis performed by Dacome *et al.* [4], in that an increase in the streamwise velocity appears above the resonator during the inflow cycle (higher-velocity flow in the TBL flow is brought down), while a decrease in streamwise velocity appears during the outflow phase (the TBL flow is displaced upwards).

B. Mean flow characteristics

We now proceed with assessing the effect of the HR on the turbulence statistics. Figures 9(a) and 9(b) show contours of the mean streamwise velocity for both the baseline case and the HR case. The mean velocity of the TBL is barely affected by the presence of the HR, with the exception of the region close above the resonator where bent isolines indicate an increase in the streamwise velocity. Differences in the mean velocity only appear deep within the linear region, which is not well resolved with the TR-PIV and better commented on in Sec. III D when evaluating the wall-shear stress.

An effect of the resonator on the flow is more evident when assessing the spatial fields of the streamwise Reynolds stress, $\overline{u'u'}$ [Figs. 9(c) and 9(d)]. An increase in the value of $\overline{u'u'}$ is apparent above the resonator, and in the streamwise–wall-normal region covered by $x^{+} = [-30, 300]$ and $y^{+} = [15, 35]$. Figures 9(e) and 9(f) show the Reynolds shear stress component, where a noticeable increase in the absolute value of $\overline{u'v'}$ appears directly above the resonator (later on it will be shown that this increase in energy is due to fluctuations at the scale of resonance). Similar observations can be made in Figs. 9(g) and 9(h), where the wall-normal Reynolds stress $\overline{v'v'}$ increases in magnitude directly above the resonator.

To better quantify the effects of the resonator on the Reynolds stresses, Figs. 10(a), 10(b), and 10(c) show the percentage difference of $\overline{u'u'}$, $\overline{u'v'}$, and $\overline{v'v'}$, respectively, between the resonator and the baseline case. Above the resonator and slightly downstream of it (until $x^{+} \approx 60$), the streamwise Reynolds stresses are amplified by up to 25% in the region below $y^{+} \approx 15$. However, downstream of the resonator, the increase in streamwise Reynolds stress shifts upwards, between $y^{+} \approx 15$ and
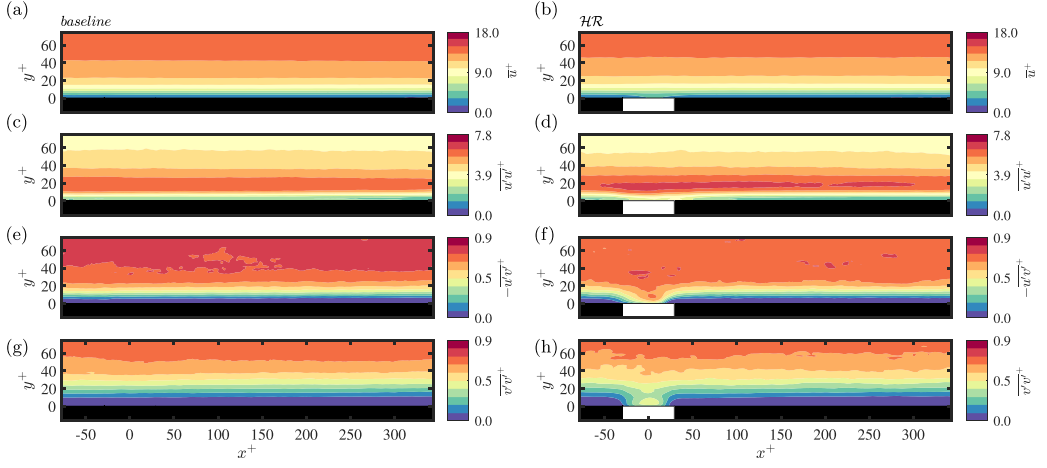
FIG. 9. (a), (c), (e), (g) Contours of (a) the mean streamwise velocity, (c) the streamwise Reynolds stress, (e) the Reynolds shear stress, and (g) the wall-normal Reynolds stress for the baseline case. (b), (d), (f), (h) Identical to subfigures (a), (c), (e), (g) but for the HR case.

$y^+ \approx 35$, and substantially reduces in intensity by roughly 5.5%. Interestingly, close to the wall, a reduction of $\overline{u'u'}$ of up to 15% appears. Similarly, we find an increase of both the Reynolds shear stresses and the wall-normal Reynolds stresses directly above the resonator's orifice, extending to a wall-normal height of $y^+ \approx 25$, and a streamwise distance of $x^+ \approx 100$. This increase is followed by a 15% attenuation of both Reynolds stresses after the resonator, extending up to a wall-normal height of $y^+ \approx 60$ and a streamwise distance of $x^+ \approx 300$.
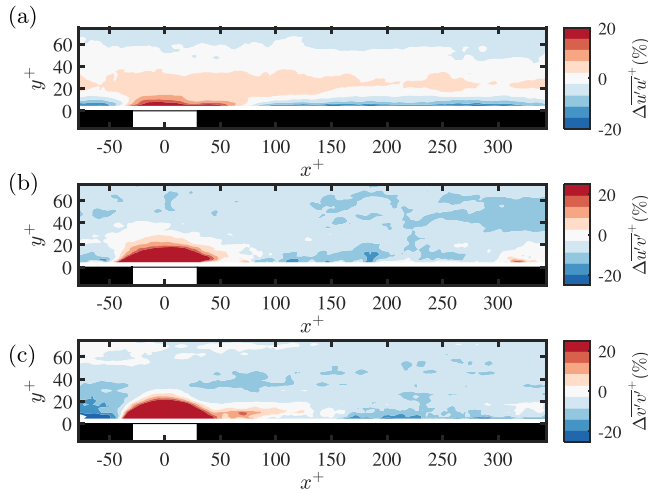

FIG. 10. Contour of the percentage difference of (a) the streamwise Reynolds stress $\overline{u'u'}$, (b) the Reynolds shear stress $\overline{u'v'}$, and (c) the Reynolds wall-normal stress $\overline{v'v'}$ of the case where the HR is embedded with respect to the baseline case.
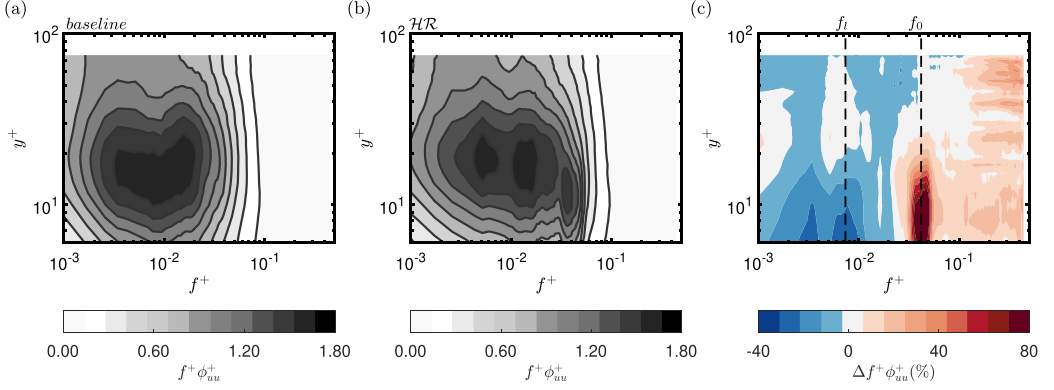
FIG. 11. (a), (b) Premultiplied energy spectrograms of the streamwise velocity fluctuations, $f^+\phi_{uu}^+$ at $x^+ = 100$, for (a) the baseline case and (b) the HR case. (c) Percentage difference of the energy spectrograms presented in subfigures (a) and (b): a positive (red) value indicates a larger energy content in the HR case.

C. Spectral energy of turbulent velocity fluctuations

A spectral analysis of the velocity fluctuations allows for a detailed inspection of how the resonator alters the energy content of the TBL flow across different turbulent scales. Figure 11(a) shows the spectrogram of streamwise velocity fluctuations for the baseline case, with alongside in Fig. 11(b) the altered spectrogram downstream of the resonator, at $x^+ = 100$. To highlight changes between them, their percentage difference is plotted in Fig. 11(c). A narrow-band increase in energy of u is seen around the resonance frequency. This region of increased energy is confined to $y^+ \lesssim 30$ at this downstream location and comprises an energy intensification of up to 80%. In addition, the resonator amplifies the energy of smaller scales (i.e., higher frequencies) at super resonance, up to 20%. Most notably, a broader band of energy attenuation is observed at larger scales (i.e., lower frequencies) and with an attenuation reaching up to 40%. The $u'v'$ cospectrogram and the v' spectrogram is presented in Figs. 12 and 13, respectively, in an identical way as the u' spectrum in Fig. 11. Observations are also similar for both: a strong energy amplification appears around the resonance scale, which continues (to a lesser degree) at the scales beyond resonance. Most interestingly, large-scale energy attenuation residing at the subresonance band of frequencies also appears in the Reynolds shear stress, with similar levels of attenuation up to 40%.
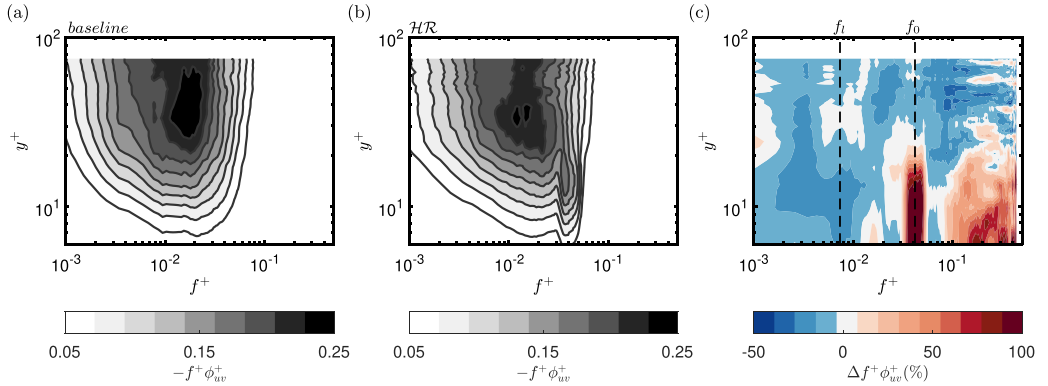

FIG. 12. Identical to Fig. 11 but for the cospectrogram, $-f^+\phi_{uv}^+$ at $x^+ = 100$, instead of the $f^+\phi_{uu}^+$ spectrogram.
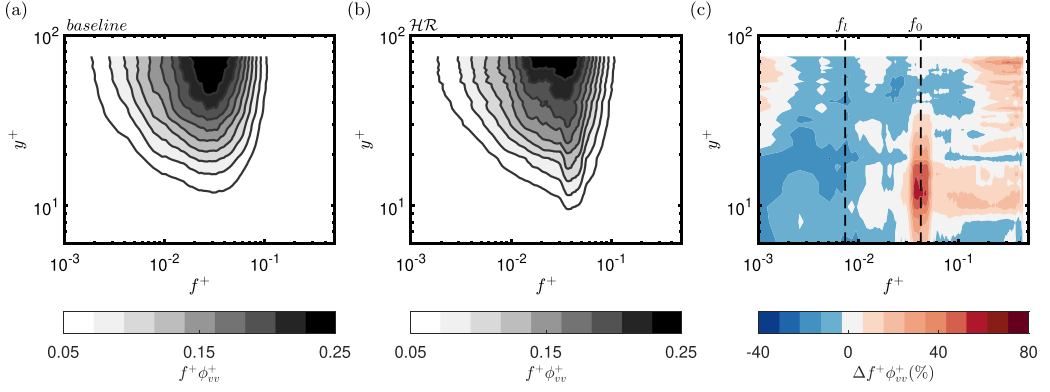
FIG. 13. Identical to Fig. 11 but for the v spectrogram, $f^+\phi_{vv}^+$ at $x^+ = 100$, instead of the $f^+\phi_{uu}^+$ spectrogram.

We now proceed by examining two frequencies of the streamwise velocity fluctuations, centered at $f_l^+ = 0.006$ (subresonance) and $f_0^+ = 0.04$ (resonance). Spatial distributions of the energy content at those two frequency bands are shown in Figs. 14(a) and 14(b), respectively. The effect of the HR on the spatiospectral distribution can be enhanced by observing the percentage difference of the energy relative to the baseline case. This is presented in Figs. 14(c) and 14(d), corresponding to the absolute energy contours shown in Figs. 14(a) and 14(b), respectively. Notably, at resonance, there is a narrow plume-type region of energy increase, which persists up to a downstream distance of at least $x^+ = 250$. On the contrary, the large-scale energy in u fluctuations is attenuated in the region close to the wall. It also becomes apparent that resonance scales that are amplified decay considerably faster than the degree by which the larger scales recover from an energy attenuation. For instance, the resonator increases the energy of the scales around the resonance frequency by more than 100% above the resonator. That energy increase decays and reaches a value of 5% by $x^+ = 200$. However, the attenuation in energy returns to the value of the baseline case much further downstream as it goes from 30% at $x^+ = 75$ to 20% at $x^+ = 300$. Furthermore, these effects are confined to distinct regions in wall-normal direction: Resonance-related fluctuations occupy a region up to $y^+ = 20$ [Fig. 14(d)], while the bulk of the effects on the attenuated scales is confined to a thin, elongated region below $y^+ \approx 10$. The latter region seems to extend far beyond the captured flow region (e.g., $x^+ \gg 300$).
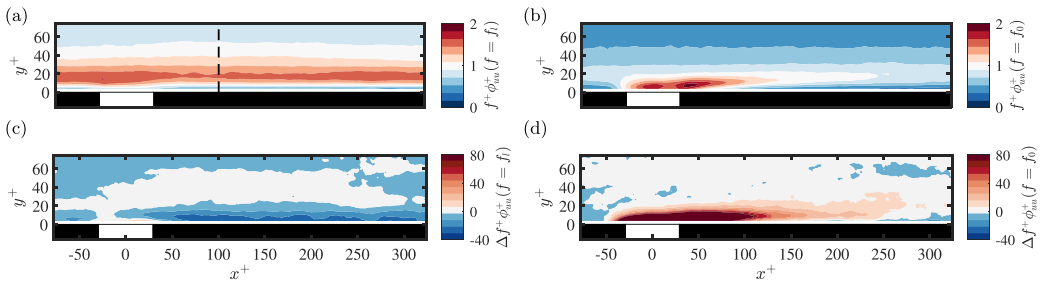

FIG. 14. (a), (b) Contours of the spatial distribution of the premultiplied streamwise energy $f^+\phi_{uu}^+$ for the resonator case at $f_l^+ = 0.006$ and $f_0^+ = 0.04$, respectively; the dashed line indicates the streamwise location of the spectrograms in Fig. 11. (c), (d) Contours of the percentage difference of the streamwise energy at f_l^+ and f_0^+, respectively, for the HR case relative to the baseline case.
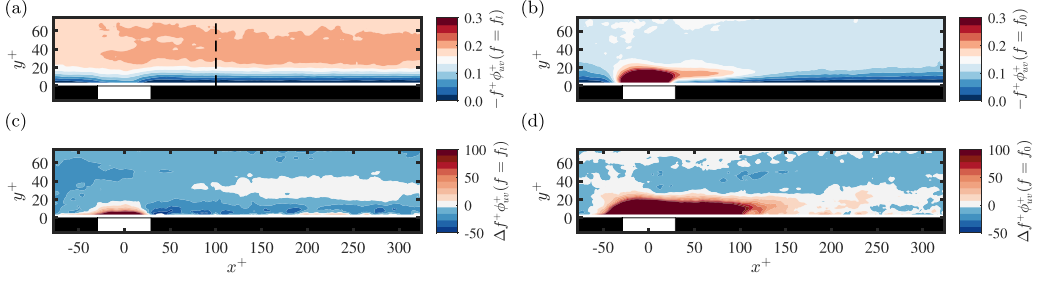
FIG. 15. (a), (b) Contours of the spatial distribution of the premultiplied energy cospectrogram $-f^+\phi_{uv}^+$ for the resonator case at $f_l^+ = 0.006$ and $f_0^+ = 0.04$, respectively; the dashed line indicates the streamwise location of the cospectrogram in Fig. 12. (c), (d) Contours of the percentage difference of the premultiplied energy cospectrogram $-f^+\phi_{uv}^+$ at f_l^+ and f_0^+, respectively, for the HR case relative to the baseline case.

Similarly, we analyze the spatial distributions of the premultiplied cospectrogram of $u'v'$ at the same two frequency bands considered earlier, of f_l^+ and f_0^+, in Figs. 15(a) and 15(b), respectively. At resonance, a more round and notably shorter plume region can be observed in comparison to the one observed in Fig. 14(b). Additionally, in Fig. 15(a) an observable thickening of the near-wall contour levels downstream of the resonator's orifice indicates a reduction of the energy.

Figures 15(c) and 15(d) show the percentage difference of $u'v'$ fluctuation energy for, again, the same f_l^+ and f_0^+ frequencies. Compared to the effects of the resonator on the streamwise energy at resonance, the amplification of $u'v'$ fluctuation energy is more intense and occupies a higher wall-normal distance ($y^+ < 30$) and a shorter streamwise extent as the amplification of energy decays to 5% at $x^+ = 160$. Much like the energy attenuation in u fluctuations, this behavior is confined to $y^+ \lesssim 10$ and extends far beyond the captured flow region.

Spatial distributions of the premultiplied energy spectrogram of v fluctuations, at the same two frequency bands considered earlier (f_l^+ and f_0^+), are presented in Figs. 16(a) and 16(b), respectively. At resonance, the HR case exhibits a more concentrated plume region directly above the resonator's orifice. Figure 16(a) shows a thickening of the near-wall contour levels downstream of the resonator, similar to the one observed in Fig. 15(b).

When concentrating on the percentage difference of $f\phi_{vv}$ it is observed that for resonance frequency f_0^+ the intensification region occupies a wall-normal distance of ($y^+ \lesssim 40$), and a similar streamwise extent of that observed in Fig. 15(d). As for the energy attenuation, it appears to occupy
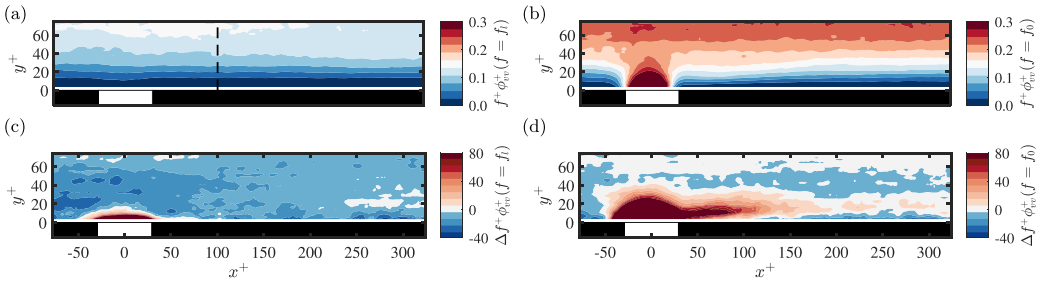

FIG. 16. (a), (b) Contours of the spatial distribution of the premultiplied energy spectrogram $f^+\phi_{vv}^+$ for the resonator case at $f_l^+ = 0.006$ and $f_0^+ = 0.04$, respectively; the dashed line indicates the streamwise location of the spectrogram in Fig. 13. (c), (d) Contours of the percentage difference of the premultiplied energy spectrogram $f^+\phi_{vv}^+$ at f_l^+ and f_0^+, respectively, for the HR case relative to the baseline case.
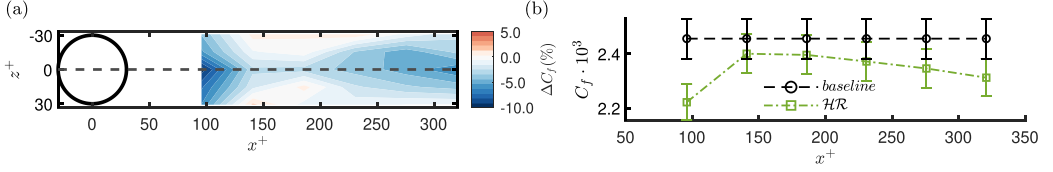
FIG. 17. (a) Contour of the percentage difference of the skin-friction coefficient of the case with the HR embedded with respect to the baseline TBL. (b) Variation of the skin-friction coefficient in the streamwise direction of the case with the HR embedded in comparison to the average skin-friction coefficient of the baseline TBL.

a larger wall-normal extent than that of the one observed in Fig. 14(c) and extends well beyond the area where the flow is captured.

D. Changes of skin-friction drag downstream of the resonator

A field of the local wall-shear stress downstream of the HR was mapped out with OFI. Figure 17(a) shows the contour of the percentage difference of the skin-friction coefficient for the case with the HR embedded, with respect to the baseline TBL. Alongside, in Fig. 17(b), a detailed streamwise profile of C_f is shown at the spanwise center, $z = 0$. At the downstream position closest to the resonator, i.e., $x^+ = 95$, the reduction in C_f is maximum in the spanwise center, reaching approximately 8%. Further downstream, a recovery of C_f occurs whereby the skin-friction coefficient increases by a value of roughly 2%, with respect to the baseline case, at off-center spanwise locations near $z^+ = -30$ and $z^+ = 30$. The region of recovery is then followed by another region of C_f decrease with values up to 6%. A slight asymmetry can be observed across the $z^+ = 0$ line (this, however, falls within the uncertainty bounds of the measurements and is thus considered negligible).

The observed initial region of skin-friction drag reduction is thought to be a wake effect due to velocity streamlines stagnating in the orifice of the resonator. Nevertheless, in the second region, the skin-friction drag reduction is presumably linked to the reduction in turbulent shear stress, both of which extend beyond our measurement domain.

IV. RESONANCE-TURBULENCE INTERACTION MECHANISM

It has become evident that the resonator has a frequency-dependent effect on grazing velocity fluctuations. We posit that the HR's impedance condition at the orifice must play a direct role in the resonator-turbulence interaction mechanism. To elucidate the mechanism, and in particular the one leading to large-scale attenuation, the incoming velocity fluctuations of the TBL flow are compared to the velocity perturbations of the resonator. In addition, pressure fluctuations need to be considered given that (i) they are related to the velocity perturbations of the resonator at the orifice, through its frequency-dependent impedance, and (ii) they are inherently coupled with velocity fluctuations in the incoming flow. For the latter, Luhar *et al.* [22] and Jafari *et al.* [23] observed that the phase difference between the wall-normal velocity and the pressure is $\pi/2$ in a TBL.

Before being able to relate the TBL flow and resonator perturbations, it remains a question of what energy source in the flow excites the resonator. An assessment of the energy budget of the wall-normal velocity variance within the resonator's orifice sheds light on this issue. Shahzad *et al.* [24] performed such an assessment for acoustic liners in a turbulent channel flow. They found how the energy in the wall-normal velocity fluctuations within the orifice is not extracted from the mean flow but rather distributed from energy within the pressure fluctuations just above the resonator. This implies that within the view of a mass-spring-damper resonator system, the pressure fluctuations are the forcing of the system, while the wall-normal velocity fluctuations are the response.
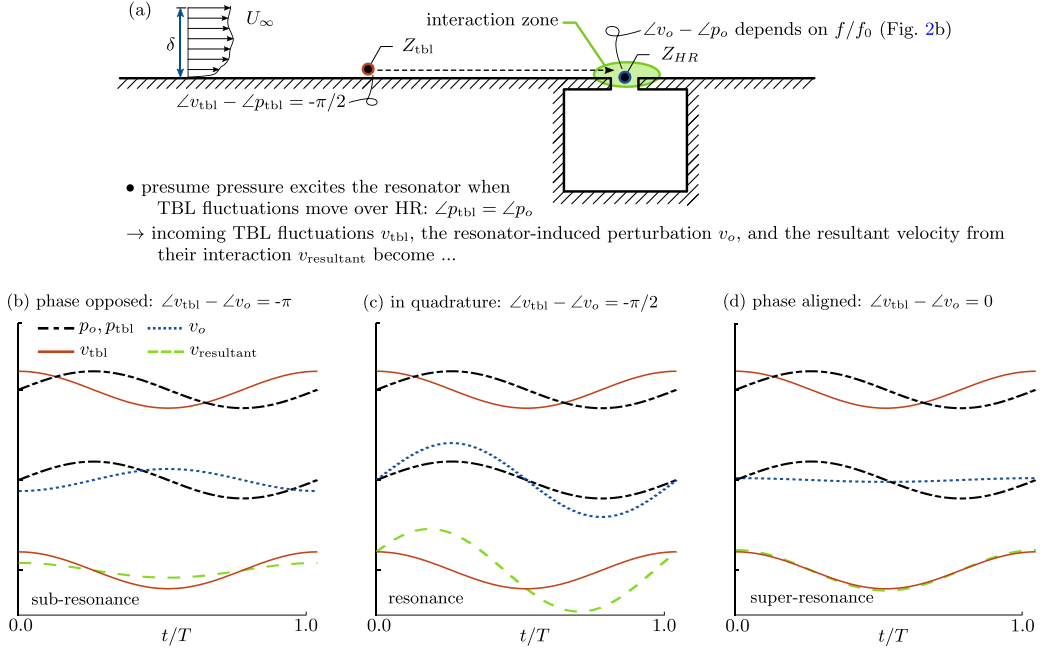
FIG. 18. (a) Schematic of the incoming TBL (with impedance relation Z_{tbl}) and the wall-embedded HR (impedance relation $Z_{\mathcal{HR}}$ at the orifice) over which the resonator-turbulence interaction occurs. (b), (c), (d) Illustrations of harmonic fluctuations over one period (p_{tbl}, v_{tbl}, v_o, $v_{\text{resultant}}$) for a frequency residing at subresonance, resonance, and super-resonance; note that T denotes the wave period of each respective case.

We now proceed by considering the resonance-turbulence interaction mechanism at a scale of subresonance, resonance, and superresonance. The mechanism we propose assumes that the interaction between the turbulence and resonance is predominately linear. Therefore, within close proximity of the resonator's orifice, the resultant velocity fluctuation will be a type of summation of the incoming velocity fluctuation and ones induced by the resonator. Figure 18 depicts the amplitude and phase response of the wall-normal velocity at the resonator's orifice (v_o) in comparison to the pressure (p_{tbl}) and wall-normal velocity (v_{tbl}). At subresonance [Fig. 18(b)] the oscillatory pressure of the incoming flow and resonator are shown with the black dash-dotted line. Given the respective phase relations of velocity, with v_{tbl} leading the pressure cycle by $\pi/2$ and v_o lagging the pressure cycle by $\pi/2$, it becomes evident that v_o is in *phase opposition* to the incoming vertical velocity fluctuation of the TBL flow, v_{tbl}. This presumably causes the attenuation of velocity fluctuation intensity seen in $v_{\text{resultant}}$, which is the resultant of the resonator-turbulence interaction. When following the same reasoning, v_o and v_{tbl} fluctuations are in *phase quadrature* at resonance; the amplitude of v_o is high due to resonance, leading to energy amplification in $v_{\text{resultant}}$ [Fig. 18(c)]. Finally, at super-resonance, v_o and v_{tbl} fluctuations are in *phase alignment*, but the magnitude of v_o is negligible due to the viscous damping at those frequencies, leading to a considerably lower energy amplification than at resonance [Fig. 18(d)].

In order to support the proposed resonator-turbulence interaction model, a visualization of convective turbulent fluctuations is presented at a temporal scale of subresonance and resonance. For this purpose, a conditional average of the spatial field of v fluctuations is conducted and is denoted as $\widetilde{v}(x, y, t)$. This type of temporal average considers a temporal signal constructed from the wall-normal velocity fluctuations, box-averaged over a spatial domain above the resonator (dotted box shown in Figs. 19(a) and 19(b). First, a bandpass with a window that extends $\pm 20\%$ of the chosen frequency (f_l^+ and f_0^+) is applied to the temporal signal. Secondly, peaks within
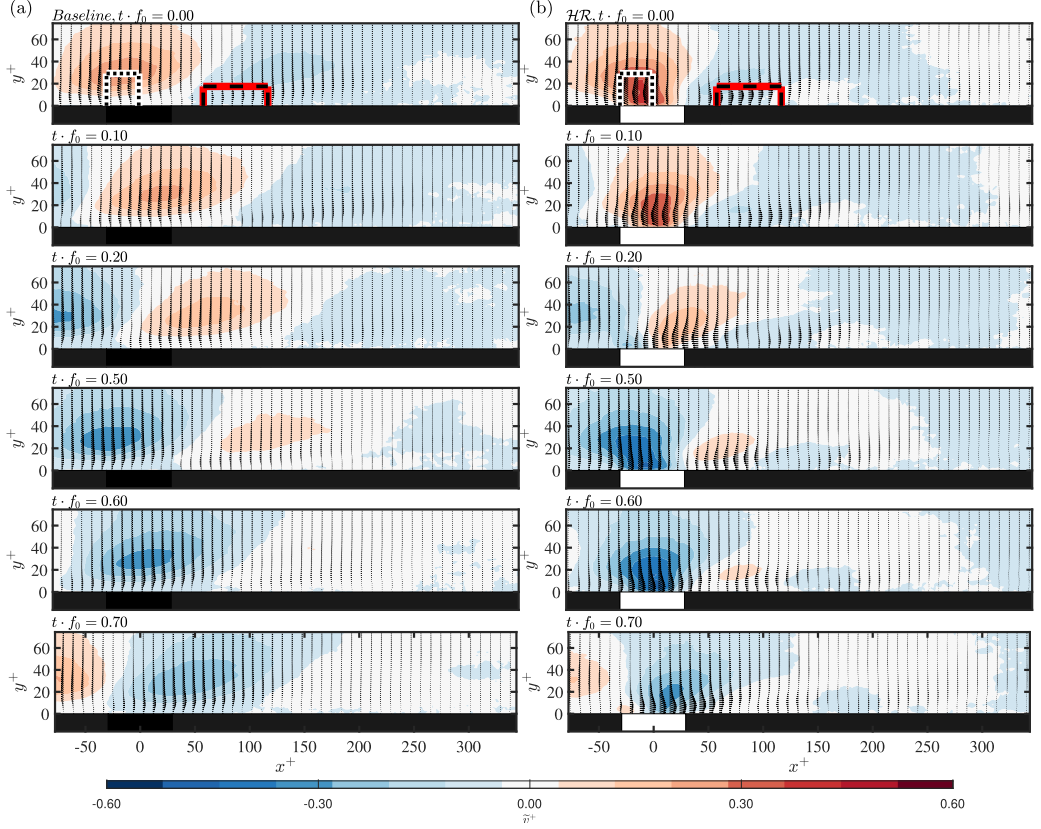
FIG. 19. Six instances of the conditionally averaged wall-normal velocity fluctuation around resonance ($f_0^+ = 0.04 \pm 0.0024$) for (a) the baseline case in the left column and (b) the HR case in the right column. The dotted box indicates the position of the box-average signal used for conditioning the conditional average, and the dashed red box indicates the averaging area of wall-normal velocity fluctuation for generating the plots in Fig. 21.

the filtered signal were identified (thus corresponding to instances of strong upward velocity) and appeared relatively periodic due to the narrow-band spectral filter. Then, 15 equispaced bins were defined from peak to peak, and all instantaneous velocity fields were assigned to the respective bins. Bin-averaging of these fields then yields the conditionally averaged wall-normal velocity fields, $\widetilde{v}(x, y, t \cdot f_i)$, with $t \cdot f_i \in [0, 1)$, with a temporal resolution of 15 fields in one period corresponding to the chosen frequency, f_i.

Figure 19 presents six instances of the conditionally averaged wall-normal velocity fluctuation around resonance ($f_0^+ = 0.04 \pm 0.0024$), for the baseline case and the one with the HR embedded. Figure 20 presents data in an identical manner but now considers a large-scale v fluctuation corresponding to the subresonance frequency, $f_l^+ = 0.006 \pm 0.0024$ ($f_l/f_0 = 0.15$). A video of the conditionally averaged streamwise and wall-normal velocity fluctuations around resonance, for both the baseline case and the one with the HR embedded is provided. Additionally, a similar video but focusing on large-scale velocity fluctuations, corresponding to the subresonance frequency f_l^+, is available in the Supplemental Materials [25] and [26], respectively. A substantial increase of the intensity in $\widetilde{v}$ is observed downstream of the resonator around resonance, in comparison to the baseline case. This increase is confined in the streamwise direction, as it returns to the baseline level in the region beyond $x^+ = 250$. This reflects the earlier observation on the basis of the
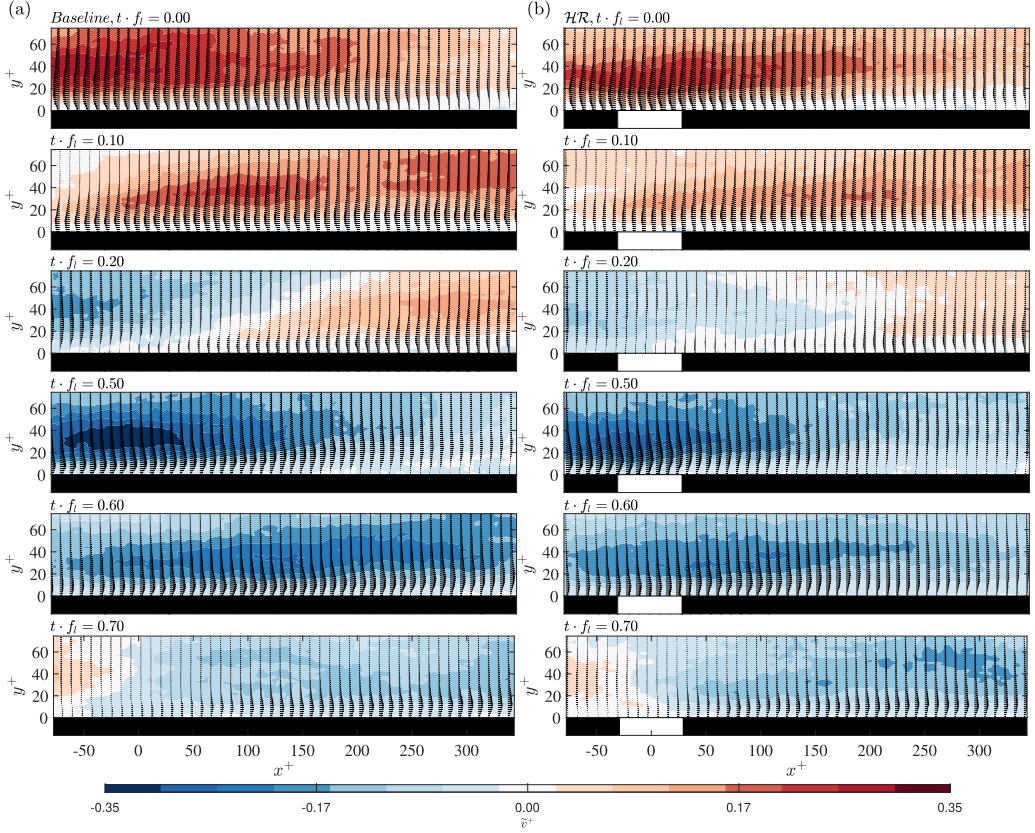
FIG. 20. Six instances of the conditionally averaged wall-normal velocity fluctuation at subresonance ($f_l^+ = 0.006 \pm 0.0024$) for (a) the baseline case in the left column and (b) the HR case in the right column.

energy spectrograms. In addition, the velocity structures above the resonator appear to be rounder in shape and have a lower inclination angle. At subresonance a notable decrease is observed in the conditionally averaged streamwise velocity fluctuations downstream of the resonator, for at least the streamwise region captured in our current measurements, $x^+ \in [0, 350]$. Further research is required to examine the total spatial extent by which the large-scale energy is attenuated.

We proceed by examining the relative phase and amplitude behavior of the wall-normal velocity fluctuations behind the resonator. These can be seen in Fig. 21, where the conditionally averaged wall-normal velocity fluctuation $\tilde{v}^+$ was box averaged (red dashed box shown in Figs. 19(a) and 19(b), and plotted across different instances for subresonance, resonance, and super-resonance frequencies. The behavior of the wall-normal velocity fluctuations is in agreement with the predicted trend of the posited interaction model between resonance and turbulence (shown in Fig. 21).

Following our hypothesis and discussions of supporting results, a single HR with grazing, broadband velocity fluctuations will in any circumstance (i) amplify energy at the resonance frequency, and at the frequency band beyond it, and (ii) attenuate energy at frequencies below resonance. Though, when the resonator is tuned to a natural frequency that is much beyond $f^+ = 1/25$, the attenuation in the large-scale energy seems to be of a lower percentage at a downstream position of $x^+ = 100$, as observed by Dacome $et\ al.$ [4]. Future research should shed further light on this issue. In addition, future efforts should assess the pressure drag penalty due to the presence of the orifice and link the reduction in the wall-shear stress to the off-the-wall modification of the turbulent velocity fluctuations.
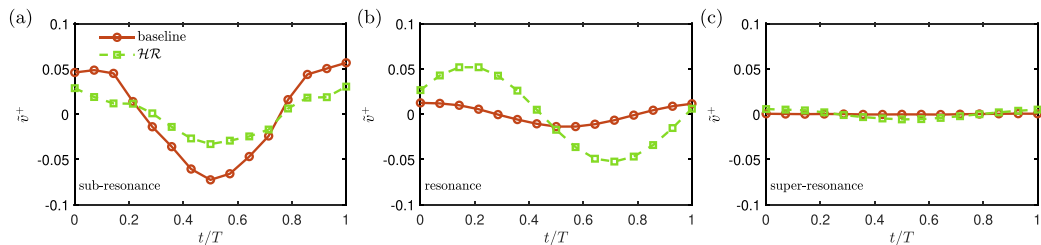
FIG. 21. Conditionally averaged wall-normal velocity fluctuation, spatially averaged over the red box indicated in Figs. 19(a) and 19(b). For each plot one period in time is considered for fluctuations of a frequency residing at (a) subresonance, (b) resonance, and (c) super-resonance.

V. CONCLUDING REMARKS

This study investigated the interaction of a single Helmholtz resonator with wall-bounded turbulence with the aim of understanding the physics associated with resonance-turbulence interactions. In this work we took an experimental approach where time-resolved planar particle image velocimetry was employed at a friction Reynolds number of $\mathrm{Re}_\tau \approx 2300$ as the primary tool of investigation. The resonator's natural frequency is designed to match the peak frequency of the wall-pressure spectrum, resulting in the excitation of scales near and above resonance while attenuating the energy of subresonant scales. This attenuation is attributed to the local impedance at the resonator's orifice. The proposed interaction mechanism relates the pressure fluctuations of the incoming TBL flow to the induced velocity fluctuations at subresonance, resonance, and super-resonance. The resultant velocity fluctuation close to the resonator seems to be the resultant of a superposition of the incoming velocity fluctuation and the resonator-induced one. Thus, Helmholtz resonators with their resonance frequency near the peak frequency of the wall-pressure spectrum are potentially applicable to attenuate near-wall, large-scale turbulence content over a range of friction Reynolds numbers, provided that the viscous scaling is maintained. Finally, future work has to address whether this interaction is governed by viscous-scaled parameters. Our fundamental understanding of passive resonator-induced modifications in the wall-impedance condition offers insights into designing surfaces for effective skin-friction drag control, potentially advancing the field toward practical applications for wall-shear stress manipulation.

ACKNOWLEDGMENTS

[1] R. L. Panton, K. P. Flynn, and D. G. Bogard, Control of turbulence through a row of Helmholtz resonators, in *25th AIAA Aerospace Sciences Meeting, Reno, NV, USA* (AIAA, 1987), AIAA Paper 1987-0436.

[2] K. P. Flynn, R. L. Panton, and D. G. Bogard, Effect of Helmholtz resonators on boundary-layer turbulence, AIAA J. **28**, 1857 (1990).

[3] K. P. Flynn and R. L. Panton, The interaction of Helmholtz resonators in a row when excited by a turbulent boundary layer, J. Acoust. Soc. Am. **87**, 1482 (1990).

[4] G. Dacome, R. Siebols, and W. J. Baars, Small-scale Helmholtz resonators with grazing turbulent boundary layer flow, J. Turbul., 2412586 (2024).

[5] J. Jiménez and A. Pinelli, The autonomous cycle of near-wall turbulence, J. Fluid Mech. **389**, 335 (1999).

[6] A. J. Smits, B. J. McKeon, and I. Marusic, High-Reynolds number wall turbulence, Annu. Rev. Fluid Mech. **43**, 353 (2011).

[7] M. Lee and R. D. Moser, Direct numerical simulation of turbulent channel flow up to $Re_\tau = 5200$, J. Fluid Mech. **774**, 395 (2015).

[8] R. L. Panton, M. Lee, and R. D. Moser, Correlation of pressure fluctuations in turbulent wall layers, Phys. Rev. Fluids **2**, 094604 (2017).

[9] Y. Tsuji, J. H. M. Fransson, P. H. Alfredsson, and A. V. Johansson, Pressure statistics and their scaling in high-Reynolds-number turbulent boundary layers, J. Fluid Mech. **585**, 1 (2007).

[10] J. C. Klewicki, P. J. A. Priyadarshana, and M. M. Metzger, Statistical structure of the fluctuating wall pressure and its in-plane gradients at high Reynolds number, J. Fluid Mech. **609**, 195 (2008).

[11] R. L. Panton and J. M. Miller, Excitation of a Helmholtz resonator by a turbulent boundary layer, J. Acoust. Soc. Am. **58**, 800 (1975).

[12] M. Alster, Improved calculation of resonant frequencies of Helmholtz resonators, J. Sound Vib. **24**, 63 (1972).

[13] U. Ingard, On the theory and design of acoustic resonators, J. Acoust. Soc. Am. **25**, 1037 (1953).

[14] R. L. Panton and J. M. Miller, Resonant frequencies of cylindrical Helmholtz resonators, J. Acoust. Soc. Am. **57**, 1533 (1975).

[15] W. J. Baars, G. Dacome, and M. Lee, Reynolds-number scaling of wall-pressure–velocity correlations in wall-bounded turbulence, J. Fluid Mech. **981**, A15 (2024).

[16] A. Sciacchitano, F. Scarano, and B. Wieneke, Multi-frame pyramid correlation for time-resolved PIV, Exp. Fluids **53**, 1087 (2012).

[17] H. H. Fernholz, G. Janke, M. Schober, P. M. Wagner, and D. Warnack, New developments and applications of skin-friction measuring techniques, Meas. Sci. Technol. **7**, 1396 (1996).

[18] A. Segalini, J. D. Rüedi, and P. A. Monkewitz, Systematic errors of skin-friction measurements by oil-film interferometry, J. Fluid Mech. **773**, 298 (2015).

[19] G. C. Zilliac, Further developments of the fringe-imaging skin friction technique, NASA Technical Memorandum NASA-TM-110425 (NASA, 1996).

[20] N. Hutchins, T. B. Nickels, I. Marusic, and M. S. Chong, Hot-wire spatial resolution issues in wall-bounded turbulence, J. Fluid Mech. **635**, 103 (2009).

[21] See Supplemental Material at http://link.aps.org/supplemental/10.1103/PhysRevFluids.9.114610 for a video of the instantaneous streamwise velocity fluctuation u'^+, the instantaneous wall-normal velocity v^+, and simultaneous time series of the cavity pressure and wall-normal velocity across the orifice.

[22] M. Luhar, A. S. Sharma, and B. J. McKeon, On the structure and origin of pressure fluctuations in wall turbulence: Predictions based on the resolvent analysis, J. Fluid Mech. **751**, 38 (2014).

[23] A. Jafari, B. J. McKeon, and M. Arjomandi, Frequency-tuned surfaces for passive control of wall-bounded turbulent flow – A resolvent analysis study, J. Fluid Mech. **959**, A26 (2023).

[24] H. Shahzad, S. Hickel, and D. Modesti, Turbulence and added drag over acoustic liners, J. Fluid Mech. **965**, A10 (2023).

[25] See Supplemental Material at http://link.aps.org/supplemental/10.1103/PhysRevFluids.9.114610 for a video of the conditionally averaged streamwise and wall-normal velocity fluctuations around resonance f_0^+ for both the baseline case and that with the HR embedded.

[26] See Supplemental Material at http://link.aps.org/supplemental/10.1103/PhysRevFluids.9.114610 for a video of the conditionally averaged streamwise and wall-normal velocity fluctuations around the sub-resonance frequency f_l^+ for both the baseline case and that with the HR embedded.